Characterization of a polymer-based, fully organic prosthesis for implantation into the subretinal space of the rat

Maria Rosa Antognazza, Mattia Di Paolo, Diego Ghezzi, Maurizio Mete, Stefano Di Marco, José Fernando Maya-Vetencourt, Rita Maccarone, Andrea Desii, Fabio Di Fonzo, Mattia Bramini, Angela Russo, Lucia Laudato, Ilaria Donelli, Michele Cilli, Giuliano Freddi, Grazia Pertile, Guglielmo Lanzani, Silvia Bisti, Fabio Benfenati

Abstract

Replacement strategies arise as promising approaches in case of inherited retinal dystrophies leading to blindness. A fully organic retinal prosthesis made of conjugated polymers layered onto a silk fibroin substrate is engineered. First, the biophysical and surface properties are characterized; then, the long-term biocompatibility is assessed after implantation of the organic device in the subretinal space of 3-months-old rats for a period of five months. The results indicate a good stability of the subretinal implants over time, with preservation of the physical properties of the polymeric layer and a tight contact with the outer retina. Immunoinflammatory markers detect only a modest tissue reaction to the surgical insult and the foreign body that peaks shortly after surgery and progressively decreases with time to normal levels at five months after implantation. Importantly, the integrity of the polymeric layer in direct contact with the retinal tissue is preserved after five months of implantation. The recovery of the foreign-body tissue reaction is also associated with a normal b-wave in the electroretinographic response. The results demonstrate that the device implanted in nondystrophic eyes is well tolerated, highly biocompatible, and suitable as retinal prosthesis in case of photoreceptor degeneration.

Introduction

Inherited retinal dystrophies, such as Retinitis pigmentosa (RP), are among the most prevalent causes of blindness.(1) Despite enormous efforts in the clinical treatment of many eye diseases, no established method to prevent or cure photoreceptor degeneration has been as yet identified. As an alternative to pharmacological treatments, gene therapy, stem cell transplantation or optogenetics, many groups are attempting to restore vision in advanced forms of RP with retinal prostheses to reactivate the spared retinal network by electrical stimulation.(2, 3) One approach (epiretinal implants) consists in the direct stimulation of retinal ganglion cells (RGCs), while the other consists in implanting the prosthesis in place of photoreceptors (subretinal implants), thus taking advantage of the processing activity of the inner retina. The latter approach has been proposed based on the evidence that the morphology of the inner retinal cells could be relatively preserved for extended periods of time.(4)

During the past two decades, several devices, with different working principles, have been described as retinal prostheses.(5) However, one of the common limitations of current retinal prosthesis is the need of trans-ocular cables to provide power supply and control signals. The design of silicon-based photovoltaic retinal implants successfully solved the need of interconnections between the implanted intraocular chip and extraocular devices.(6) However, silicon-based devices remain relatively stiff, if compared to the Young modulus of the retina; in turn, this may enhance the development of a foreign-body reaction in the proximity of the implant, eventually leading to the device encapsulation by fibrotic tissue that considerably hinders its functionality.

The suitability of conjugated polymers (CPs) as building blocks of a photovoltaic interface with living cells and retina explants has been recently documented by several groups.(7) We demonstrated that CPs maintain their activity in contact with electrolyte solutions, and that neurons can be effectively grown onto these materials. Upon illumination, modulation of the electrical activity of primary neurons cultured on the polymer surface was observed.(8) Subsequently, we demonstrated that the very same organic device in subretinal configuration was able to restore light sensitivity in explants of blind degenerate retinas.(9) This approach has many advantages with respect to silicon-based prostheses, namely higher biocompatibility, higher flexibility, and mechanical compliance.

The device tested in vitro was fabricated on glass with a first conductive layer of indium-tin oxide (ITO) and a superficial layer of CPs (regioregular poly(3-hexylthiophene)/rrP3HT alone or blended with phenyl-C61-butyric acid methyl ester/PCBM) in direct contact with the tissue and/or the extracellular medium.(8, 9) In order to engineer a fully organic device for in vivo implantation, we replaced ITO with poly(3,4-ethylenedioxythiophene)-poly(styrenesulfonate) (PEDOT:PSS) and used silk fibroin (SF) as substrate for the polymeric layers. Fibroin, the protein

component of silk, is an established biomaterial that has a long history of clinical applications including sutures and biological scaffolds for tissue repair and regeneration.(10) Fibroin has excellent and tunable properties in terms of biocompatibility and partial biodegradability. Implanted silk scaffolds were shown to be well tolerated and to elicit only mild inflammation and immune responses. The bendability, compatibility with polymer deposition techniques, resistance to sterilization procedures, and moderate rigidity of SF comply with the trans-scleral subretinal implantation procedure.(10) Indeed, a preliminary study carried out with a control silk-only device to test the surgical technique revealed that the morphology of the retina was highly preserved up to two months after implantation.(11)

Here, we characterized the biophysical properties of the engineered silk/polymer device and evaluated the consequences of the in vivo implantation in the subretinal space of a nondystrophic rat eye. We found that the subretinal implant is stable up to five months after surgery, with a tight contact between the polymeric layer and the outer retina and a modest tissue inflammatory reaction progressively decreases over time. These findings testify the high biocompatibility of the implant and pave the way to their long-term use in implantology.

Results and discussion

Preparation and characterization of silk substrates

An outline of the device fabrication procedure is reported in Figure 1A. Substrates were realized by casting the SF solution on top of Teflon Petri dishes that, differently from other materials (plastic, glass, aluminum), allowed getting flexible and relatively robust substrates. During solvent evaporation, one side remained exposed to air, while the other one was in contact with the Petri dish. SF is characterized by a high conformational variability, which results from the presence of various silk polymorphs, namely Silk I–III. Silk I is the natural form of fibroin, as emitted from the Bombyx mori silk glands. Being metastable, it can be easily converted to the more stable Silk II structure by mechanical, chemical or thermal treatments. Silk II refers to the arrangement of fibroin molecules in spun silk, which has greater strength and is usually considered responsible for the remarkable mechanical properties of fibroin. Silk III is referred to the silk in proximity to the air/water and/or organic/water interface. The three isoforms are characterized by precise structural properties and, most interestingly to the goal of this work, by a different degree of crystallinity. Depending on the crystallization conditions (solvent, solution concentration, temperature, drying rate, substrate type), Silk I and/or Silk II structures are usually obtained in films deposited by solution. However, the polymorph composition can be further tuned by changing the specific parameters of subsequent processing. It was therefore important to check how and

to what extent the contact with water, the treatment with organic solvents, the thermal annealing processes, and finally the sterilization procedure affect the pristine chemical/physical properties of the as-casted silk films (SF samples). We investigated these effects by means of Fourier-transform IR absorption (FTIR) and differential scanning calorimetry (DSC) experiments, throughout all the subsequent phases of prosthesis fabrication, i.e.: (i) first PEDOT:PSS conducting layer deposition, followed by annealing (SP1 and SP1a samples); (ii) second PEDOT:PSS deposition and further annealing (SP2a); (iii) P3HT deposition and final annealing (SPP and SPPa samples).

The FTIR profile (Figure 1B) of the SF film cast from aqueous solution is typical of an amorphous SF material, with prevailing random coil (r.c.)/Silk I molecular conformation.(12) It is worth noting that, in the FTIR spectrum, r.c. and Silk I bands are almost undistinguishable because they fall very close to each other. The amorphous character of the film is evidenced by the position and shape of Amide I (broad peak at 1626 cm^{-1}), Amide II (peak at 1508 cm^{-1}, shoulder at about 1530 cm^{-1}), and Amide III (peak at 1224 cm^{-1}) bands, attributed to peptide bond vibrations. Accordingly, the lower intensity bands falling in the skeletal range at 1100–900 cm−1, attributable to vibrations of the side chain groups, display the characteristic profile of amorphous SF films. The DSC profile (Figure 1C) of the same sample confirms the above comments. The main conformationally sensitive thermal transitions are the baseline deflection at 175 °C, marking the glass transition temperature Tg of SF, and the exothermic peak at 212 °C, which is attributed to rearrangement and crystallization of amorphous SF chains. These two thermal events can be observed only in amorphous SF films.(13) The two other strong endothermic transitions at about 100 and 286 °C are due to evaporation of moisture and thermal degradation of SF chains, respectively. The wettability of the two sides of the SF thin film was clearly different, showing a variation in the contact angle of almost 25° between the side exposed to open air (70° ± 5°) and the one exposed to Teflon (94° ± 8°).

To facilitate the coating process and get more uniform layers, PEDOT:PSS was deposited on the more hydrophobic side, exposed to Teflon. The deposition of the first PEDOT:PSS layer (SP1) onto the SF film surface caused only slight changes of the SF film structure, which remained prevalently amorphous. In fact, the FTIR spectrum recorded in the attenuated total reflection (ATR) mode was closely similar to that of the untreated SF film (Figure 1B). Accordingly, the DSC thermogram still displayed the crystallization peak at 212 °C, although with a lower intensity (Figure 1C). This feature, together with the fact that Tg is no more detectable, can be attributed to a decrease in SF chain mobility that is probably caused by the partial chain rearrangement occurring during the swelling/drying cycle associated with deposition of the PEDOT:PSS layer. The first thermal treatment subsequent to PEDOT:PSS deposition (SP1a) did not modify the molecular conformation of the SF film that, on the basis of the FTIR spectrum, remained mostly amorphous (Figure 1B). However, the SF chain thermal mobility became more restricted, as

indicated by the further decrease in intensity of the 212 °C crystallization peak (Figure 1C). Conversely, the deposition of the second PEDOT:PSS layer and its annealing treatment (SP2a) induced a conformational transition from r.c./Silk I to Silk II, as revealed by the changes in the Amide I, II, and III bands, as well as by minor changes observed in the skeletal range of the FTIR spectrum of the sample. Typical β-sheet bands appeared at 1690, 1616, and 1254 cm^{-1};(12) both Amide I and II bands became sharper, as a consequence of the decrease in intensity of various vibrational modes attributed to r.c., type II β-turns, and other turns and bends falling in the 1670–1630 cm^{-1} range, which usually contribute to band width broadening (Figure 1B).(14) The β-sheet crystallization was also confirmed by the remarkable thermal stability observed in the 150–250 °C temperature range (Figure 1C). Finally, the deposition of rr-P3HT (SPPna), followed by thermal treatment (SPPa), did not lead to further significant changes in the structure of the SF film, which had already achieved a high degree of stability, typical of the Silk-II conformation.

Optoelectronic and Microscopic Characterization of the Retinal Implant

To verify whether the optoelectronic properties of the semiconducting layer were preserved during processing and maintenance in a saline environment, the polymer optical absorption, the photocurrent action spectrum and the photocurrent dynamics were measured immediately after fabrication (Day 0) and one month later (Day 30) (Figure 2). Samples were immersed in a 0.2 m NaCl aqueous solution kept at 37 °C and exposed to environmental light/dark cycles of 12 h. To avoid bacterial proliferation, the solution was sterilized by microfiltration and changed every 3 d. One month after fabrication, the device displayed an optical absorption spectrum that was virtually identical to that of the as-casted films, and typical of a rr-P3HT thin film, with absorption maximum at 520 nm and vibrational replicas at 550 and 605 nm, consistent with the semicrystalline nature of the polymer film (Figure 2A).

No significant changes were also observed in the photocurrent dynamics. The positive signal observed at the onset of illumination is consistent with a current flowing from the PEDOT:PSS/P3HT device to the counter-electrode through the electrolyte. The current decays back to zero during the light pulse, with a decay time constant in the order of few ms. Upon switching off the light, an opposite signal is observed, attributable to a capacitive discharging of the polymer/electrolyte interface. Notably, ion-doping phenomena of the organic layers, possibly occurring upon prolonged contact with the water environment, did not lead to relevant changes in the transient photocurrent behavior, and the dynamics of the capacitive signal were not minimally affected by keeping the device under physiological condition for 30 d (Figure 2B).(15) One month after fabrication, the contact angle measured on the silk surface did not considerably vary with respect to

the fresh device (67° ± 5° vs 59° ± 8°), meaning that the wettability of silk exposed to air or saline water remains essentially the same (Figure 2C). Conversely, the polymer surface, one month after fabrication, became much more hydrophilic, with a contact angle comparable to the one measured on the silk-side of the prosthetic device (51 ± 11°) (Figure 2C). These results are a positive indication of the fact that the prosthetic implants, once inserted into the subretinal space, could be sufficiently permeable, and should guarantee an adequate degree of oxygenation to the underlying retinal pigment epithelium (RPE).

Scanning electron microscopy (SEM) imaging was employed to assess the fine surface structure and the possible changes occurring in the device architecture upon time. Images acquired immediately after preparation of the prosthesis (Figure 2D) show that the PEDOT:PSS layer optimally conforms to the soft silk substrate. The two subsequent depositions are not clearly distinguishable, and PEDOT:PSS formed a unique, finely interconnected layer, with an overall thickness of ≈550 nm. The adhesion between the rr-P3HT active polymer (≈200 nm thickness) and the PEDOT:PSS layer was also optimal. The images of the device acquired at day 0 confirm the suitability of the spin coating parameters employed for the deposition of both PEDOT:PSS and rr-P3HT. When the samples were kept under physiological conditions (i.e., exposed to saline solution and illuminated under ambient light at 37 °C) for one month, a very good degree of adhesion of the polymeric layers to the substrate was still observed (Figure 2E) in the absence of clear swelling of the conducting and/or semiconducting layers is evidenced on a microscopic scale. On a macroscopic scale, the overall surface of the device appears more corrugated after one month than immediately after preparation, but samples were intentionally left free to rearrange their conformation in the absence of any mechanical constraint. Once implanted in the subretinal space, this effect would be presumably decreased as a consequence of the intraocular pressure.

Evaluation of Implant Stability and Retina Reaction

The retinal device was implanted in the subretinal space of healthy RCS-rdy+/Lav rats through a scleral flap (Figure 3A). Indirect ophthalmoscopy, near-infrared confocal scanning laser ophthalmoscopy (cSLO) and spectral domain ocular coherence tomography (OCT) scans performed at various times after implantation showed that the implant, centrally localized within the fundus (Figure 3B,C), remained fixed in its position over time. Retinal integrity was preserved over and around the implant, in the absence of any noticeable degenerative effect, and no swelling or delamination of the device was observed (Figure 3D).

One of the main concerns regarding the potential long-term functioning of the organic device as a retinal prosthesis was the integrity of the surface polymeric layer over time. Although in vitro data (see Figure 2) suggest a substantial preservation

of the polymer properties, shear stresses and prolonged contact with the inflammatory environment could promote polymer delamination or degradation. To ascertain the persistence of the active layer, we exploited the intrinsic fluorescence of P3HT. Representative retina images from sections that underwent full processing for immunohistochemistry, including chemical fixation, cryopreservation, and slicing (all processes that may cause breakage, delamination or relocation of the polymer) showed that the implants remained in contact with the inner retina and were covered by a fairly intact the polymeric layer up to five months after surgery (n = 9; Figure S1A–D, Supporting Information). When the polymeric coverage of the silk substrate was quantified one (n = 7) and five (n = 9) months after surgery, about 80% of the silk substrate surface was coated with the polymer at both times, indicating that, while the surgical implant and early postimplant phase are critical for polymer cracking/delamination, the polymer is quite stable afterward (Figure S1E, Supporting Information).

To evaluate the morphological changes induced in the retina by the implant, implanted and sham-operated retinas were subjected to histochemical analysis 7, 30, and 150 d postimplant (DPI). As previously reported, the photoreceptor layer underwent degeneration due to retina/RPE detachment in correspondence of the implant, while the inner retina, after a transient period of edema (<1 month) returned to normal (Figure 4).(16), (17) The reduction in the outer nuclear layer (ONL) thickness superior to the implant is likely attributable to the mechanical stress during the surgery. Accordingly, one week after surgery, some degree of edema was observed in the ONL of the implanted region, representing a clear sign of the activation of an inflammatory response.

Reactive gliosis is a sensitive indicator of retinal stress and represents an attempt to protect retinal tissue, limit tissue remodeling, and promote repair.(18) Glial fibrillary acidic protein (GFAP) immunoreactivity (Figure 5) increased immediately after surgery both in the implanted and in the peripheral regions, reached its peak one month after surgery and decreased thereafter to return to baseline five months after surgery. This pattern of response coincides with a transient stress reaction of the retina due to the insertion of a foreign body that regresses after five months from the surgery.

The retina has the ability to activate protective mechanisms in response to damaging stimuli, including upregulation of cytokines and in trophic factors such as fibroblast growth factors (FGFs). Specifically, FGF2 is expressed by Muller cells and RGCs during adulthood and, upon mechanical stress, is upregulated and translocates from glial cells to photoreceptor somata.(19) After surgery, the FGF2 response significantly increased by exhibiting a dual inner–outer and implant-peripheral gradient (Figure 6). One week after surgery, FGF2 was upregulated in the RGC layer with an implant-to-periphery gradient, probably due to the implant-

induced mechanical stress at the retina/vitreous interface. In the implant region, an increase of FGF2 was also detectable in the Muller cell bodies. One month from surgery, FGF2 expression in RGCs decreased, suggesting recovery from the mechanical stress at the retina/vitreous body interface, while a concomitant translocation of FGF2 to the photoreceptor layer was observable. This event was particularly evident in the portions of retina peripheral to the implant, whereas it was less pronounced in correspondence of the implant, likely because of the reorganization and thinning of the photoreceptors layer. Similar to what observed for GFAP expression, FGF2 immunoreactivity returned back to baseline five months after surgery.

Under physiological conditions, microglial cells are restricted to the inner retina where they are involved in immunological surveillance, clearance of the debris, and maintenance of retina homeostasis.(20) In response to a stress, microglia quickly increases in number, and starts migrating toward the site of injury. The insertion of the implant immediately triggered microglial activation, evaluated by immunoreactivity for ionized Ca^{2+}-binding adapter molecule-1 (Iba1), with a significant increase in the cell number and cell migration toward the ONL (Figure 7). This activation was particularly evident in the implanted area 7 and 30 d after surgery, whereas, in adjacent areas, the initial microglial activation rapidly decreased and disappeared. Five months after surgery, the extent of the overall microglial activation was strongly reduced, indicating a progressive recovery toward baseline, and sparse activated microglial cells only persisted in the ONL of the implanted region (Figure 7).

When the electroretinogram (ERG) response to light flashes were evaluated five months after surgery, the large majority of the implanted animals (six out of nine animals checked by OCT to confirm position and integrity of the device and of the adjacent retina) responded to the flash with a delayed b-wave of similar amplitude with respect to the controls, while three animals displayed defective responses (Figure S2C, Supporting Information). When retrospective immunohistochemical analysis was performed, animals that had a bad ERG performance also presented strong astrogliosis and microgliosis (Figure S2A,B, Supporting Information), while animals that performed well in ERG displayed a normalization of the inflammatory markers.

Conclusion

The application of organic semiconductors as photoactive materials in bio-interfaces has been recently reported. A device made of semiconducting polymers, such as P3HT or P3HT:PCBM, spin-coated over a thin film conductive ITO on glass has been recently shown to have unique properties, i.e., direct light sensitivity,

biocompatibility, ability to modulate the electrical activity of excitable and nonexcitable cells with high spatial and temporal resolution.(8) Moreover, such a device was able to rescue light sensitivity with daylight range sensitivity in explanted degenerate retinas.9 These results demonstrate that organic semiconductors can be a valid alternative to the more traditional devices used for retinal implants mostly based on inorganic semiconductors and/or metallic electrodes, exhibiting softness and conformability, light sensitivity, and no need for power supply or control signals.

The polymeric interface that we have developed is potentially an ideal substitute for the degenerated photoreceptors in RP. However, despite the claim of being tissue-friendly, the long-term compatibility of CPs with the retina tissue has never been evaluated. Thus, the above-described device was engineered to make it interface fully organic and suitable for in vivo implantation, by replacing ITO with the conductive polymer PEDOT:PSS and using SF as a highly biocompatible porous substrate (SF/PEDOT:PSS/rr-P3HT device). Indeed, SF has been widely used in biomedical applications as sutures, tissue scaffolds, hemostatic and drug delivery agents,(10) it has been recently proposed as a component of flexible electronics for recording and optical systems,(21) and was well-tolerated when subretinally implanted in the retina.(11) The SF substrate was stable throughout the processing steps necessary for the realization of the full prosthesis architecture, and the structural and physical properties of the three-layer SF/PEDOT:PSS/rr-P3HT device were not altered by a prolonged exposure to physiological temperature and salt concentrations that only increased its surface hydrophilicity.

Although CPs have been already used for biomedical applications, their future use as materials for retinal prostheses to treat blindness secondary to photoreceptor degeneration requires an assessment of the reaction of the retina toward the multicomponent implanted device over time.(7) Moreover, the status of the polymeric layer needs to be monitored, as its direct contact with inner neuronal layers is essential for the functioning of the device.(9) We investigated whether surgical implantation in the nondystrophic strain of the RCS rat could cause loss of inner retina neurons, edema, inflammation, and gliosis/fibrosis that would interfere with the retina-device interface, possibly causing delamination, degradation of the polymeric layers, and/or its encapsulation. The in vivo follow-up with cSLO and OCT revealed the stability of the implant and its persistent close association with the inner retina layers in the absence of retina detachment, chronic edema or fibrosis. Retina morphology was substantially preserved, except for the loss of photoreceptors at the site of the implant due to the dissection of photoreceptors from the RPE.(16), (17), (22)

Significant increases in GFAP, FGF, and Iba1 expression were observed in the operated eye, particularly in the area of implantation, indicative of an astrocyte, Muller cell, and microglial reaction to the implant. As reported by previous studies, normal retinas respond to chronic subretinal implantation with upregulation of GFAP expression by Muller cells and astrocytes, and reactive gliosis is a sensitive indicator of retinal stress and represents an attempt to promote tissue repair.(18) Indeed, in the implanted retina, an upregulation of the trophic factor FGF2 by Muller cells and RGCs and its translocation to the photoreceptor layer was observed at early stages after surgery, likely contributing to the late normalization of the inflammatory parameters. Similarly, microglia cells resident in the inner retina were activated in the early stages of implantation and migrated in the implanted region. However, the retina response to the surgical insult and the foreign body reaction significantly decreased over time, assuring the long-term contact of the device with the external retinal layers that is a requisite for efficacy proper functioning as retina prosthesis. Moreover, in spite of the shear stress during the surgical implantation and the inflammation and proliferation of microglial cells with their complement of lytic enzymes in the early phases after surgery, the bare polymeric layer in contact with the outer retina was largely preserved over time, supporting the long-term functionality of the implanted device.

In conclusion, the comprehensive experimental characterization shown in this report demonstrates the full biocompatibility of the organic retina prosthesis made by SF/PEDOT:PSS/P3HT for in vivo applications. In particular, we show here that the unavoidable tissue reaction to the surgical implant was limited to the areas directly affected by the surgery and displayed a virtually complete regression after 5 months and a significant persistence of the polymeric layers. In view of the high biocompatibility and reliability, we are currently implanting the three-layer device as subretinal prosthesis in the eye of blind RCS rats, an experimental model of Retinitis pigmentosa, to evaluate its functionality in rescuing light sensitivity and visual performances.

Experimental sections

Organic Retinal Prosthesis Fabrication: SF films were obtained from Bombyx mori cocoons. After degumming procedure, sericine-free fibers were dried for 3 d at temperature of 20 ± 2 °C and relative humidity of 65 ± 2%, dissolved in a saturated LiBr solution, and treated at 60 ± 2 °C for 3 h. The solution was then dissolved in distilled water, preheated at 60 °C, and filtered. Solution dialysis completely removed LiBr. The purified SF was filtered, drop-casted on Teflon Petri dishes, and dried for 2 d, obtaining SF films of 200 cm^2 area and 30 μm approximate thickness. After cleaning of substrates with acetone and isopropanol rinses, organic layers

were deposited on the side of SF thin films in contact with the Teflon Petri dish during SF casting. A water dispersion of PEDOT:PSS (Clevios PH1000; Heraeus) was prepared by adding the following additives: The cosolvent dimethylsulfoxide (9% in volume, purchased from Sigma-Aldrich) to increase the overall electrical conductivity; the cross-linker 3-glycidoxypropyltrimethoxysilane (0.9% in volume; Sigma-Aldrich) to enhance the adhesion of the PEDOT:PSS layer to the substrate and avoid delamination; the surfactant Zonyl FS-300 (0.18% in volume, Sigma-Aldrich) to promote dispersion wettability. PEDOT:PSS dispersion was then sonicated in an ultrasonic bath for 20 min, cooled at room temperature and deposited by spin coating in two identical steps (rotation speed 2000 rpm, duration 60 s). The double deposition was required to limit the dynamic interaction between the PEDOT:PSS dispersion and the underlying SF film and to yield a uniform layer. Between the first and the second deposition, and after the second deposition, the substrates underwent a thermal annealing process in air (120 °C, 10 min). A chlorobenzene solution of P3HT (15 000–45 000 molecular weight, Sigma-Aldrich, 30 g L^{-1}) was sonicated for more than 1 h and deposited on top of the PEDOT:PSS layer by a two-steps spin coating process (800 rpm, 5 s; 1600 rpm, 120 s). A final thermal annealing in glovebox (120 °C, 20 min) completed the fabrication of large area devices. Retinal implants of dimensions suitable for implantation in rats were obtained through laser-assisted cutting (Yb:KGW laser, Pharos, Light Conversion Ltd., with emission at 1030 nm, repetition rate of 500 KHz, and pulse width of 240 fs), by focusing the second harmonic beam onto the polymer-coated SF substrates, with incidence from the substrate side. Pulse energy, in the order of 200 nJ, and translation speed (0.4 mm s^{-1}) were adjusted to get a relatively sharp cut of the edges, without causing degradation to the optoelectronic properties of the active material. The prosthesis has a trapezoid geometry (1.8 mm height, 1.1 mm, and 0.55 mm parallel sides). Edges are intentionally smoothed during the laser-assisted fabrication to limit mechanical damage to the retinal layers during surgery. After fabrication, samples were subjected to ethylene oxide sterilization.

Biophysical Characterization of the Device: The wettability of the substrates prior to and after polymer deposition was characterized by using an OCA-15 optical contact angle measuring instrument (Data Physics). Static water contact angles were determined using the sessile drop method (2 μL, Milli-Q water) (n = 15). Optical absorption spectra were recorded by a Perkin-Elmer Lambda 1050 spectrophotometer in the visible range between 400 and 700 nm. Photocurrent action spectra and photocurrent temporal dynamics were acquired in a two-electrodes configuration, using a saline solution as electrolyte and a platinum wire as the counter electrode. Photocurrent temporal dynamics were amplified by an impedance amplifier (FEMTO DHPCA-100) and collected with a digital oscilloscope (Tektronix MSO4054). Light pulses (50 ms at 1 Hz) were provided by a

collimated, green LED system (Lumencor Spectra X, central wavelength $\lambda = 530$ nm). In action spectra measurements, the light from a tungsten lamp passed through a monochromator and was focused onto the sample at 0° incidence, through the PEDOT:PSS electrode. The light was mechanically chopped at 175 Hz, and the reference signal was fed to a lock-in amplifier. System calibration was performed by replacing the organic photodiode with a silicon photodiode of known efficiency and taking into account the dark current, the spectral response of the light source and the monochromator gratings. Cross-section images of the retinal prosthesis were acquired using a Zeiss SUPRA 40 field emission scanning electron microscope. FTIR spectra were recorded in the ATR mode with an α-Alpha-P spectrometer (Brucker) equipped with a diamond cell. For each sample, spectra (24 scans; spectral resolution 1.5 cm^{-1}) were collected in triplicate, normalized at 1450 cm^{-1}, and averaged. DSC measurements were performed with a Q200 calorimeter (TA Instruments), from room temperature to 500 °C, at a heating rate of 10 °C min^{-1}. Samples, 3–5 mg each, were put in an open aluminum pan and swept with N2 during the analysis.

In Vivo Implantation of the Device in the Rat: Royal College of Surgery nondystrophic congenic animals (RCS-rdy$^+$/Lav),(23) kindly provided by Dr. M. M. La Vail (Beckman Vision Center, University of California San Francisco, CA), were bred in our animal facility. RCS-rdy$^+$/Lav rats were housed under standard conditions with ad libitum access to food and water under a 12/12 h light/dark cycle. All animal manipulations and procedures were performed in accordance with the guidelines established by the European Community Council (Directive 2012/63/EU of 22 September 2010) and were approved by the Italian Ministry of Health (license 645/2015PR). Animals were implanted at the average age of 85 ± 10 d and analyzed at various time points after surgery up to 5 months. The subretinal implantation technique was as previously described with some modifications.(16) Implants were analyzed and followed up using indirect ophthalmoscopy and in vivo imaging.(24) To assess retinal responses, flash ERG was recorded in dark-adapted animals in response to light flashes of increasing intensity. A detailed description of these procedures is reported in the Supporting Information.

Histology and Immunohistochemistry: Cryostat sections obtained from the fixed eyes of implanted rats were investigated by immunohistochemistry and morphometric analysis (for details, see the Supporting Information). The ONL was measured in bisbenzimide-stained sections starting at the dorsal edge along the vertical meridian crossing the optic nerve head following a previously described procedure.(25) Measurements are expressed as ratio ONL/total retina thickness and calculated for the entire retinal section. The inner retina thickness was evaluated by measuring the distance between the RGC layer and the end of the outer plexiform layer. Cryosections were labeled for FGF2, Iba-1, and GFAP. The study was carried

out on retinal sections (from dorsal to ventral) that included the optic disc and that were collected after 1 week, 1 month, and 5 months from surgery. Morphometric analysis was performed on 7 fields/retina that were imaged, namely: 3 dorsal to the implant, 1 in the region of the implant, and 3 ventral to the implant. Acquisition parameters were kept constant throughout all the imaging session for comparison purposes and the densitometry analysis of fluorescent signals was performed using the ImageJ software. At least five animals were completely analyzed per each experimental group. Mean fluorescence intensity analysis for FGF2 and GFAP was performed using ImageJ. Iba1 cells were manually counted in each field.

Statistical Analysis: Data were expressed as means ± sem for number of sections analyzed from independent animals (n). ANOVA followed by the Tukey's post-hoc test was used. $p < 0.05$ was considered significant. Statistical analysis was carried out using OriginPro-8 (OriginLab Corp.) and Prism (GraphPad Software, Inc.).

Acknowledgements

M.R.A. and M.D.P.; S.B. and F.B. contributed equally to this work as co-first and co-last authors, respectively. The authors thank Dr. M. M. La Vail (Beckman Vision Center, University of California San Francisco, CA) for kindly providing RCS-rdy+/Lav rats; Dr. Ger Vijfvinkel (Oftavinci BV, Geervliet, The Netherlands) for manufacturing specific surgical tools; Drs. L. Criante and S. Perissinotto for help at the laser micro-machining facility; Francesca Canu, Ilaria Dall'Orto, Arta Mehilli, and Diego Moruzzo for technical assistance. The work was supported by Telethon – Italy (Grants GGP12033 to GL, FB, and SB, and GGP14022 to GP and FB); EU project FP7-PEOPLE-212-ITN 316832 "OLIMPIA" (to FB and GL); Fondazione Cariplo (project ON-IRIS 2013–0738 to MRA, GF, and DG); Compagnia di San Paolo (project ID 4191 to DG and FB), the Italian Ministry of Health (project RF-2013-02358313 to GP, GL, and FB), and Istituto Italiano di Tecnologia (prestartup project to GL and FB).

References

(1) a) C. A. Curcio, N. E. Medeiros, C. L. Millican, *Invest. Ophthalmol. Visual Sci.* 1996, 37, 1236.

b) R. H. Coleman, C. C. Chan, F. L. III Ferris, E. Y. Chew, *Lancet* 2008, 372, 1835.

c) S. G. Jacobson, A. V. Cideciyan, *N. Engl. J. Med.* 2010, 363, 1669.

d) S. Ferrari, E. Di Iorio, V. Barbaro, D. Ponzin, F. S. Sorrentino, F. Parmeggiani, *Curr. Genomics* 2011, 12, 238.

(2) a) M. M. Doroudchi, K. P. Greenberg, J. Liu, K. A. Silka, E. S. Boyden, J. A. Lockridge, A. C. Arman, R. Janani, S. E. Boye, S. L. Boye, G. M. Gordon, B. C. Matteo, A. P. Sampath, W. W. Hauswirth, A. Horsager, *Mol. Ther.* 2011, 19, 1220.

b) V. Busskamp, J. Duebel, D. Balya, M. Fradot, T. J. Viney, S. Siegert, A. C. Groner, E. Cabuy, V. Forster, M. Seeliger, M. Biel, P. Humphries, M. Paques, S. Mohand-Said, D. Trono, K. Deisseroth, J. A. Sahel, S. Picaud, B. Roska, *Science* 2010, 329, 413.

c) R. E. MacLaren, R. A. Pearson, A. MacNeil, R. H. Douglas, T. E. Salt, M. Akimoto, A. Swaroop, J. C. Sowden, R. R. Ali, *Nature* 2006, 444, 203.

d) R. A. Pearson, A. C. Barber, M. Rizzi, C. Hippert, T. Xue, E. L. West, Y. Duran, A. J. Smith, J. Z. Chuang, S. A. Azam, U. F. Luhmann, A. Benucci, C. H. Sung, J. W. Bainbridge, M. Carandini, K. W. Yau, J. C. Sowden, R. R. Ali, *Nature* 2012, 485, 99.

e) M. S. Singh, R. E. MacLaren, *Proc. Biol. Sci.* 2011, 278, 3009.

(3) a) D. R. Bertschinger, E. Beknazar, M. Simonutti, A. B. Safran, J. A. Sahel, S. G. Rosolen, S. Picaud, J. Salzmann, *Graefes Arch. Clin. Exp. Ophthalmol.* 2008, 246, 1505.

b) G. Dagnelie, *Curr. Opin. Neurol.* 2012, 25, 67.

c) Y. H. Luo, L. da Cruz, *Br. Med. Bull.* 2014, 109, 31.

d) A. T. Chuang, C. E. Margo, P. B. Greenberg, *Br. J. Ophthalmol.* 2014, 98, 852.

(4) a) R. E. Marc, B. W. Jones, C. B. Watt, E. Strettoi, *Prog. Retinal Eye Res.* 2003, 22, 607.

b) R. E. Marc, B. W. Jones, *Mol. Neurobiol.* 2003, 28, 139.

c) J. D. Weiland, A. K. Cho, M. S. Humayun, *Ophthalmology* 2011, 118, 2227.

(5) a) M. S. Humayun, J. D. Dorn, L. da Cruz, G. Dagnelie, J. A. Sahel, P. E. Stanga, A. V. Cideciyan, J. L. Duncan, D. Eliott, E. Filley, A. C. Ho, A. Santos, A. B. Safran, A. Arditi, L. V. Del Priore, R. J. Greenberg, *Ophthalmology* 2012, 119, 779.

b) R. E. MacLaren, A. Koitschev, A. Kusnyerik, J. Neffendorf, J. Nemeth, M. A. Naeem, T. Peters, J. D. Ramsden, H. Sachs, A. Simpson, M. S. Singh, B. Wilhelm, D. Wong, E. Zrenner, *Vision Res.* 2015, 111, 149.

c) H. Lorach, G. Goetz, R. Smith, X. Lei, Y. Mandel, T. Kamins, K. Mathieson, P. Huie, J. Harris, A. Sher, D. Palanker, *Nat. Med.* 2015, 21, 476.

d) E. Zrenner, *Sci. Transl. Med.* 2013, 5, 210ps16.

(6) 6K. Mathieson, J. Loudin, G. Goetz, P. Huie, L. Wang, T. Kamins, L. Galambos, R. Smith, J. S. Harris, A. Sher, D. Palanker, *Nat. Photonics* 2012, 6, 391.

(7) a) J. Clark, G. Lanzani, *Nat. Photonics* 2010, 4, 438.

b) N. Martino, D. Ghezzi, F. Benfenati, G. Lanzani, M. R. Antognazza, J. *Mater. Chem. B* 2013, 1, 3768.

c) L. Bareket-Keren, Y. Hanein, *Int. J. Nanomed.* 2014, 9, 65.

d) V. Gautam, D. Rand, Y. Hanein, K. S. Narayan, *Adv. Mater.* 2014, 26, 1751.

(8) a) M. R. Antognazza, D. Ghezzi, D. Musitelli, M. Garbugli, G. Lanzani, *Appl. Phys. Lett.* 2009, 94, 243501.

b) D. Ghezzi, M. R. Antognazza, M. Dal Maschio, E. Lanzarini, F. Benfenati, G. Lanzani, *Nat. Commun.* 2011, 2, 166.

c) N. Martino, P. Feyen, M. Porro, C. Bossio, E. Zucchetti, D. Ghezzi, F. Benfenati, G. Lanzani, M. R. Antognazza, *Sci. Rep.* 2015, 5, 8911.

(9) a) P. Feyen, E. Colombo, D. Endeman, M. Nova, L. Laudato, N. Martino, M. R. Antognazza, G. Lanzani, F. Benfenati, D. Ghezzi, *Sci. Rep.* 2016, 6, 22718.

b) D. Ghezzi, M. A. Antognazza, R. Maccarone, S. Bellani, E. Lanzarini, N. Martino, M. Mete, G. Pertile, S. Bisti, G. Lanzani, F. Benfenati, *Nat. Photonics* 2013, 7, 400.

(10) a) F. G. Omenetto, D. L. Kaplan, *Nat. Photonics* 2008, 2, 641.

b) F. G. Omenetto, D. L. Kaplan, *Science* 2010, 329, 528.

c) L. D. Koh, Y. Cheng, C.-P. Teng, Y.-W. Khin, X.-J. Loh, A.-Y. Tee, M. Low, E. Ye, H.-D. Yu, Y.-W. Zhang, M.-Y. Han, *Prog. Polym. Sci.* 2015, 46, 86.

d) B. Kundu, R. Rajkhowa, S. C. Kundu, X. Wang, *Adv. Drug Deliv. Rev.* 2013, 65, 457.

e) A. E. Thurber, F. G. Omenetto, D. L. Kaplan, *Biomaterials* 2015, 71, 145;

f) D. H. Kim, J. Viventi, J. J. Amsden, J. Xiao, L. Vigeland, Y. S. Kim, J. A. Blanco, B. Panilaitis, E. S. Frechette, D. Contreras, D. L. Kaplan, F. G. Omenetto, Y. Huang, K. C. Hwang, M. R. Zakin, B. Litt, J. A. Rogers, *Nat. Mater.* 2010, 9, 511.

g) V. Benfenati, K. Stahl, C. Gomis-Perez, S. Toffanin, A. Sagnella, R. Torp, D. L. Kaplan, G. Ruani, F. G. Omenetto, R. Zamboni, M. Muccini, *Adv. Funct. Mater.* 2012, 22, 1871.

(11) M. Di Paolo, D. Ghezzi, M. R. Antognazza, M. Mete, G. Freddi, I. Donelli, R. Maccarone, G. Pertile, G. Lanzani, F. Benfenati, S. Bisti, *Eur. J. Neurodegener. Dis.* 2015, 4, 23.

(12) P. Taddei, P. Monti, *Biopolymers* 2005, 78, 249.

(13) M. Tsukada, Y. Gotoh, M. Nagura, N. Minoura, N. Kasai, G. Freddi, J. *Polym. Sci. B* 1994, 32, 961.

(14) Q. Lu, X. Hua, X. Wang, J. A. Kluge, S. Lu, P. Cebe, D. L. Kaplan, *Acta Biomater.* 2010, 6, 1380.

(15) E. Stavrinidou, P. Leleux, H. Rajaona, D. Khodagholy, J. Rivnay, M. Lindau, S. Sanaur, G. G. Malliaras, *Adv. Mater.* 2013, 25, 4488.

(16) a) M. T. Pardue, E. B. Jr Stubbs, J. I. Perlman, K. Narfström, A. Y. Chow, N. S. Peachey, *Exp. Eye Res.* 2001, 73, 333.

b) A. Butterwick, P. Huie, B. W. Jones, R. E. Marc, M. Marmor, D. Palanker, *Exp. Eye Res.* 2009, 88, 22.

(17) a) Y. Mandel, G. Goetz, D. Lavinsky, P. Huie, K. Mathieson, L. Wang, T. Kamins, L. Galambos, R. Manivanh, J. Harris, D. Palanker, *Nat. Commun.* 2013, 4, 1980.

b) H. Lorach, J. Kung, C. Beier, Y. Mandel, R. Dalal, P. Huie, J. Wang, S. Lee, A. Sher, B. W. Jones, D. Palanker, *Invest. Ophthalmol. Visual Sci.* 2015, 56, 4644.

(18) a) A. Bringmann, P. Wiedemann, *Ophthalmologica* 2012, 227, 1.

b) B. I. Gallego, J. J. Salazar, R. Hoz, B Rojas, A. I. Ramírez, M. Salinas-Navarro, A. Ortín-Martínez, F. J. Valiente-Soriano, M. Avilés-Trigueros, M. P. Villegas-Perez, M. Vidal-Sanz, A. Triviño, J. M. Ramírez, J. *Neuroinflammation* 2012, 9, 92.

c) G. P. Lewis, S. K. Fisher, *Int. Rev. Cytol.* 2003, 230, 263.

(19) a) E. G. Faktorovich, R. H. Steinberg, D. Yasumura, M. T. Matthes, M. M. LaVail, *J. Neurosci.* 1992, 12, 3554.

b) N. Walsh, K. Valter, J. Stone, *Exp. Eye Res.* 2001, 72, 495.

(20) a) M. Karlstetter, S. Ebert, T. Langmann, *Immunobiology* 2010, 215, 685.

b) M. Karlstetter, R. Scholz, M. Rutar, W. T. Wong, J. M. Provis, T. Langmann, *Prog. Retinal Eye Res.* 2015, 45, 30.

c) A. Nimmerjahn, F. Kirchhoff, F. Helmchen, *Science* 2005, 308, 1314.

d) A. Noailles, L. Fernández-Sánchez, P. Lax, N. Cuenca, J. *Neuroinflammation* 2014, 11, 1.

(21) a) R. Capelli, J. J. Amsden, G. Generali, S. Toffanin, V. Benfenati, M. Muccini, D. L. Kaplan, F. G. Omenetto, R. Zamboni, *Org. Electron.* 2011, 12, 1146.

b) M. K. Hota, M. K. Bera, B. Kundu, S. C. Kundu, C. K. Maiti, *Adv. Funct. Mater.* 2012, 22, 4493.

(22) A. N. Adekunle, A. Adkins, W. Wang, H. J. Kaplan, J. F. de Castro, S. J. Lee, P. Huie, D. Palanker, M. McCall, M. T. Pardue, *Transl. Vis. Sci. Technol.* 2015, 4, 5.

(23) M. M. LaVail, R. L. Sidman, C. O. Gerhardt, *J. Hered.* 1975, 66, 242.

(24) J. W. Fransen, G. Pangeni, M. T. Pardue, M. A. McCall, *J. Neural Eng.* 2014, 11, 046012.

(25) K. Valter, S. Bisti, C. Gargini, S. Di Loreto, R. Maccarone, L. Cervetto, J. Stone, *Invest. Ophthalmol. Visual Sci.* 2005, 46, 1748.

Figures

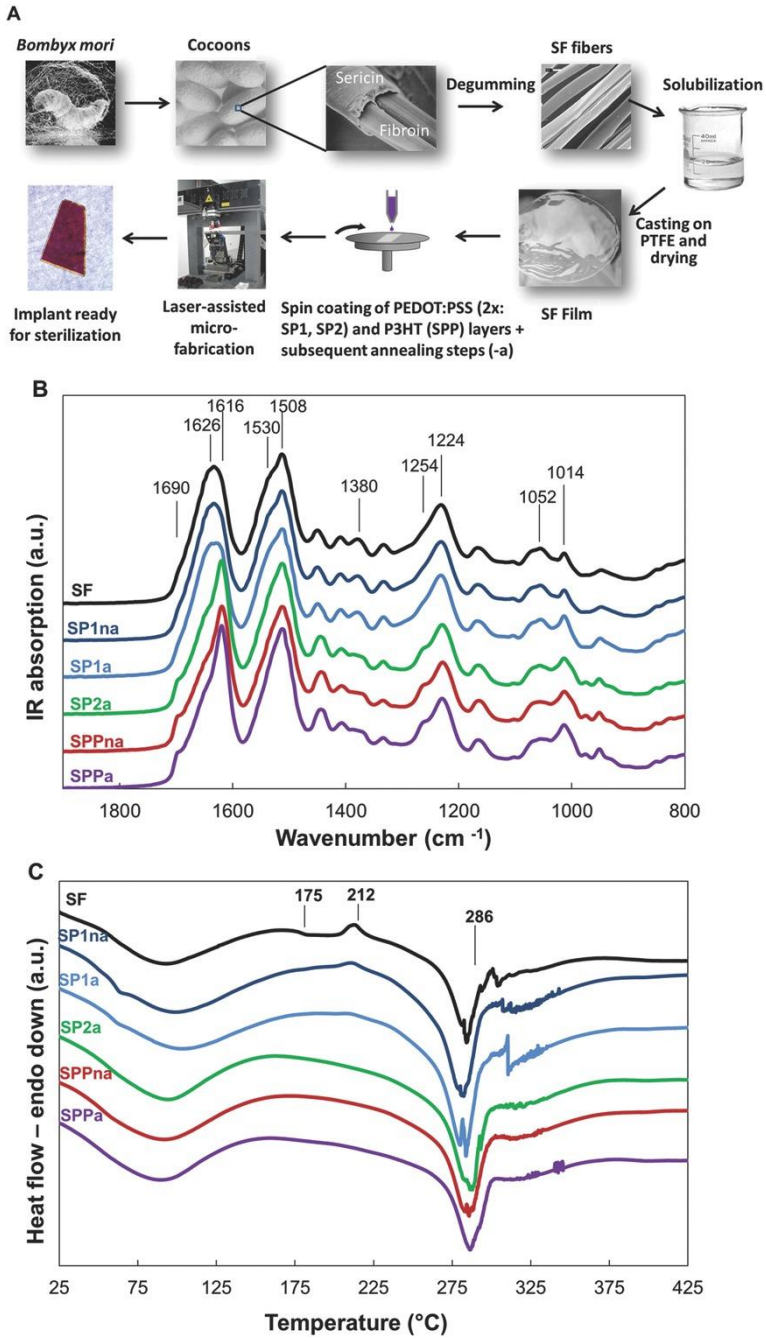

Figure 1. Retinal prosthesis fabrication and characterization. A) Schematic diagram of the device fabrication procedure. B,C) FTIR spectra (B) and DSC thermograms (C) were recorded at the different stages leading to the fabrication of the organic prosthesis. SF (black trace): silk fibroin film, as casted; SP1na (dark blue trace) and SP1a (light blue trace): silk fibroin covered by a first PEDOT:PSS layer, before and after thermal treatment in air, respectively; SP2a (green trace): silk fibroin covered by two subsequent depositions of PEDOT:PSS and annealed after each deposition; SPPna (red trace) and SPPa (purple trace): silk fibroin substrates covered by PEDOT:PSS and P3HT, before and after thermal annealing, respectively, under nitrogen atmosphere (120 °C for 20 min).

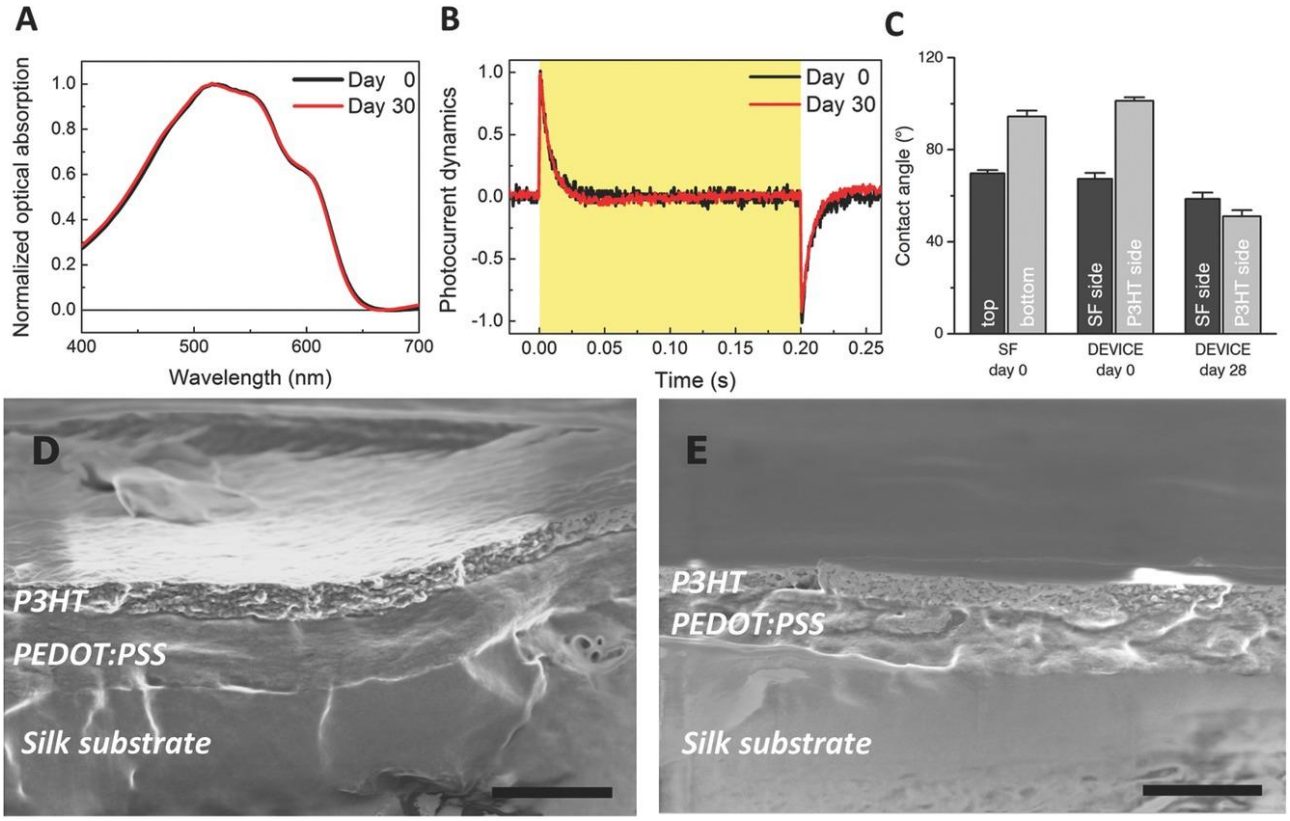

Figure 2. Structural and physical properties of the device exposed to physiological conditions. A) Optical absorption spectra recorded immediately after preparation of the device (black line) and after one month (red line) under conditions mimicking the physiological environment (0.2 m NaCl at 37 °C with ambient light). B) Photocurrent dynamics recorded immediately after preparation of the device (black line) and after one month (red line) under the same physiological conditions as described for panel (A). The shaded area represents the duration of the light stimulus. C) Water contact angles (means ± SD; n = 15) of silk substrates and full polymer implants immediately after fabrication (black) or after one month in which they were maintained at 37 °C at ambient light in saline solution (gray). SF: silk fibroin measured on the side exposed to air (top) and to the teflon surface (bottom) during fabrication. Device: three-layered SF/PEDOT:PSS/rr-P3HT device measured on the silk and polymeric surface, respectively. PEDOT:PSS and rr-P3HT were intentionally deposited on the bottom side of the silk substrate. D,E) Ultrastructure of the organic device. D) Representative cross-sectional SEM images were taken immediately after preparation and after 30 days under physiological conditions (0.2 m NaCl at 37 °C with ambient light. E) The two organic layers, composed of PEDOT:PSS and P3HT, can be clearly distinguished on the silk substrate. n = 5–6 sample devices were analyzed from two independent fabrication sessions. Scale bar, 1 μm.

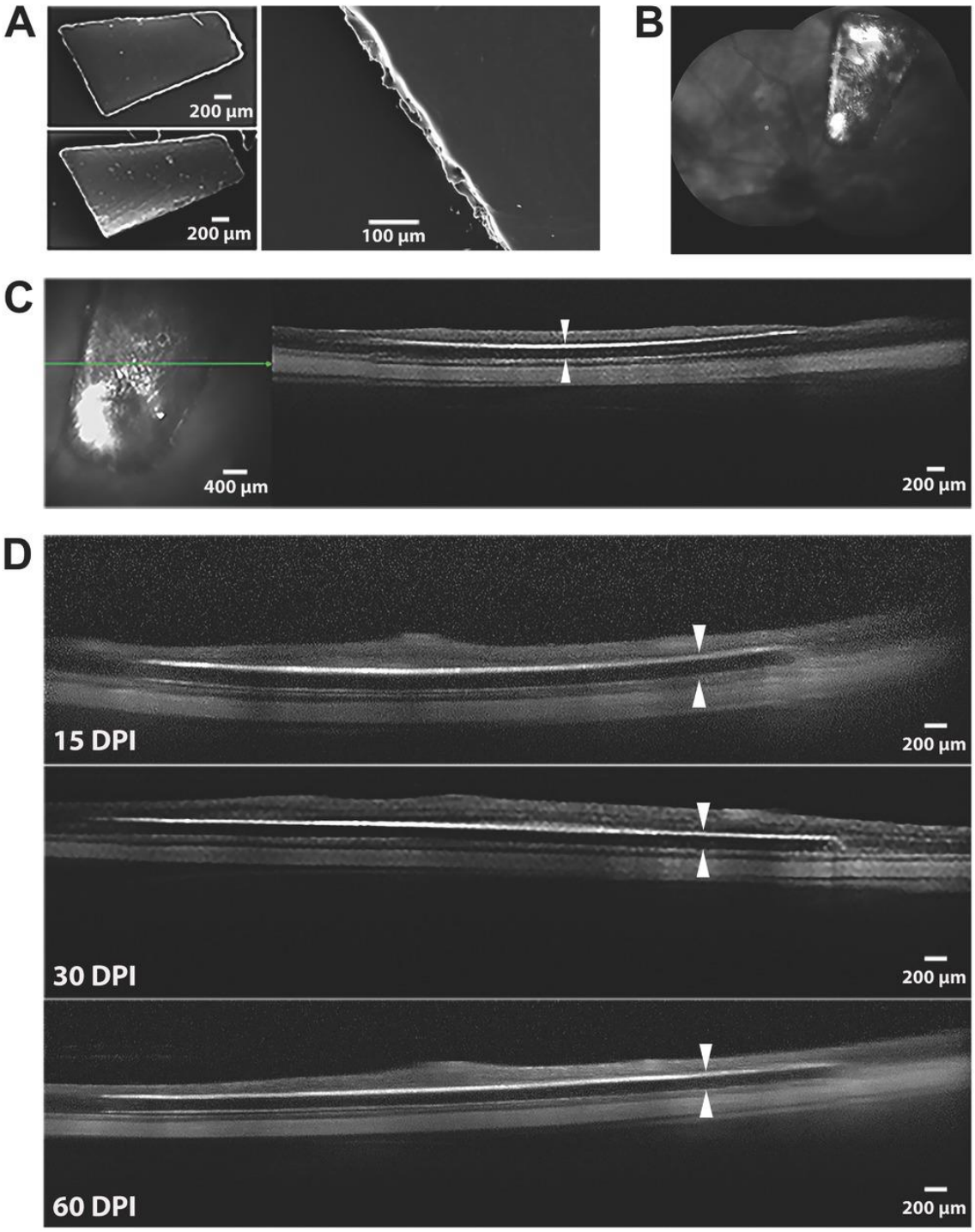

Figure 3. In vivo imaging of the retinal prosthesis. A) Low-magnification SEM images of the device before implantation. The images show the polymeric layer (top left), the back silk surface (bottom left) and a higher magnification of the laser-cut device edge (right). B) Representative cSLO image of the prosthesis subretinally implanted in the eye of an RCS-rdy rat, taken 30 d after surgery. C) Representative OCT image of the subretinally implanted prosthesis depicted in panel (B). The green line on the near-infrared image on the bottom-left corresponds to the OCT scan shown on the right. D) Temporal sequence of OCT scans acquired 15, 30, and 60 d after surgery from the implanted eye of an RCS-rdy rat. DPI, days postimplant. Arrowheads in panels (C,D) indicate the position of the device.

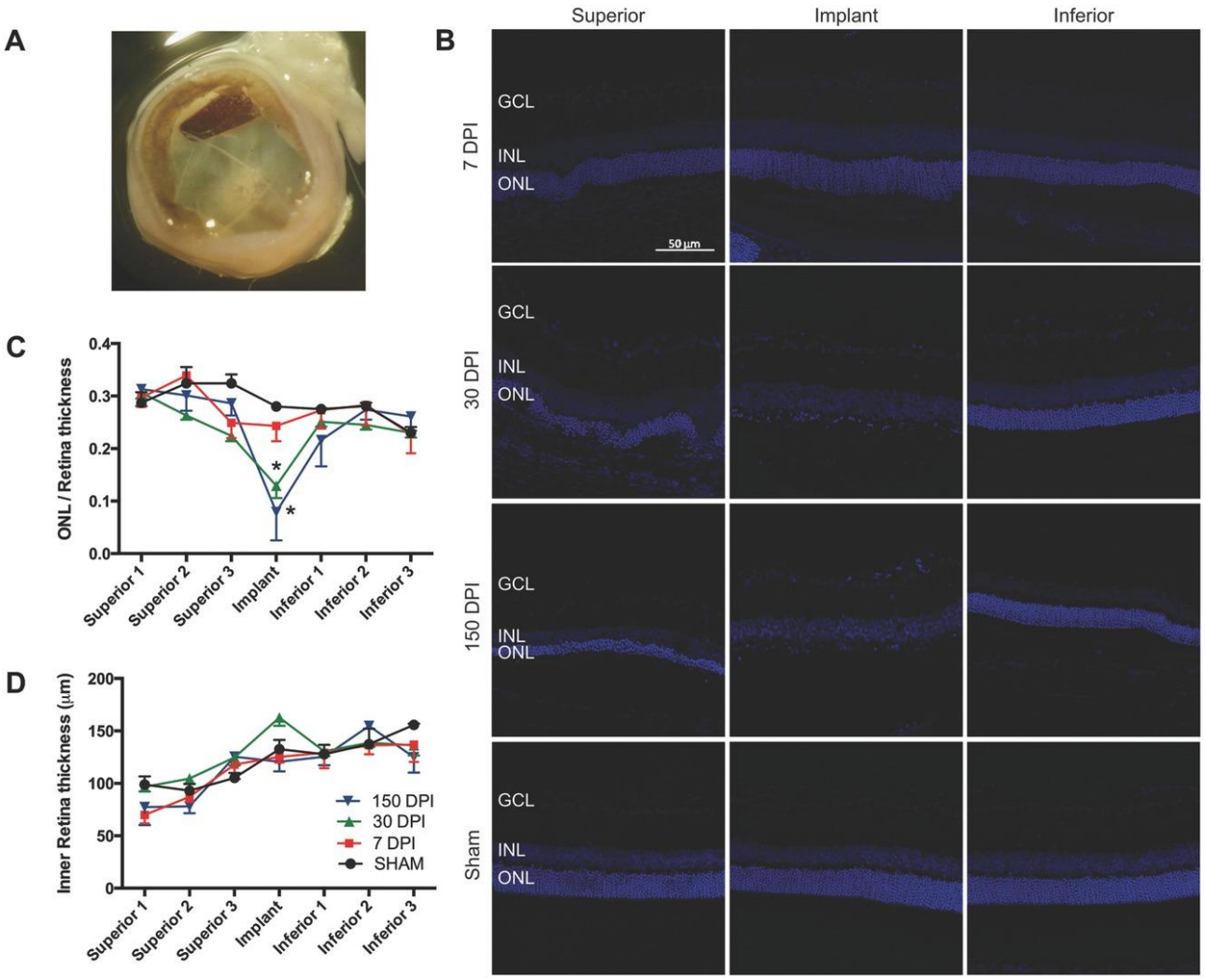

Figure 4. Effects of the prosthetic implant on retina thickness. A) View of the eye bulb after fixation shows the position and integrity of the polymeric implant. B) Reconstruction of vertical sections of implanted and control retinas collected 7, 30, and 150 DPI, and labeled with bisbenzimide. Images were acquired from corresponding fields in the various retinas by taking the implant as reference point. C) Impact of the surgery on the ratio between ONL thickness and total retinal thickness, calculated in superior, implanted, and inferior fields. D) Impact of the surgery on inner retina thickness measured in superior, implanted, and inferior fields. One-way ANOVA/Tukey's test (n = 9 per experimental group). * $p < 0.05$ versus respective control. ONL, outer nuclear layer; INL, inner nuclear layer; GCL, ganglion cell layer.

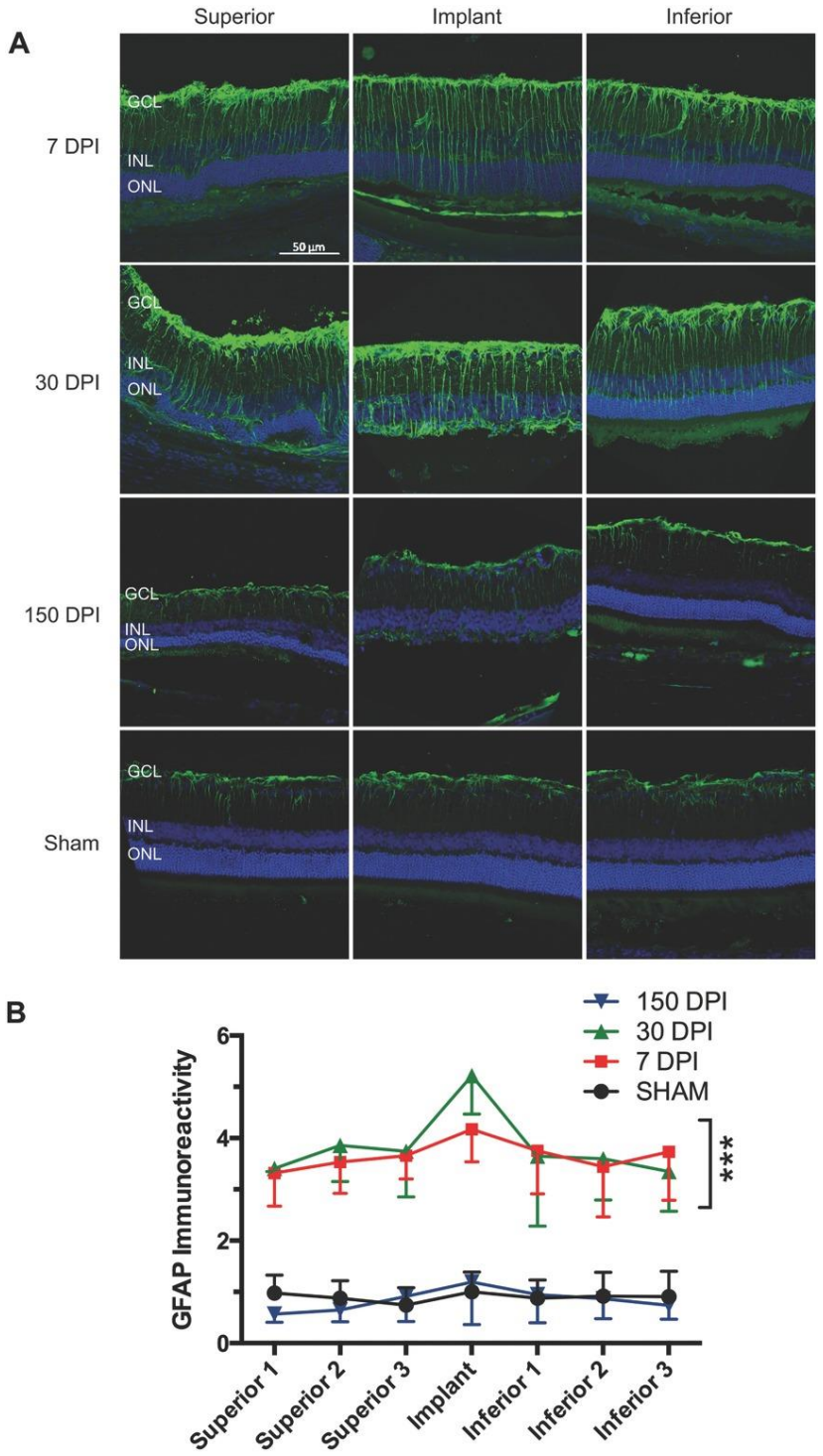

Figure 5. Effects of the prosthetic implant on GFAP expression in the retina. A) Reconstruction of vertical section of implanted retina stained for GFAP. Retinas were collected 7, 30, and 150 DPI. Images were acquired from corresponding fields in the different retinas by taking the implant as reference point. GFAP expression was upregulated after surgery and its expression peaked 1 month after surgery and normalized at later times. B) The fluorescence intensity, measured throughout the retina, shows highly significant differences in GFAP immunoreactivity at 7 and 30 DPI compared with either sham-operated or implanted animals at 150 DPI. One-way ANOVA/Tukey's test (n = 9 per experimental group). *** $p < 0.001$ versus respective controls or 150 DPI. ONL, outer nuclear layer; INL, inner nuclear layer; GCL, ganglion cell layer.

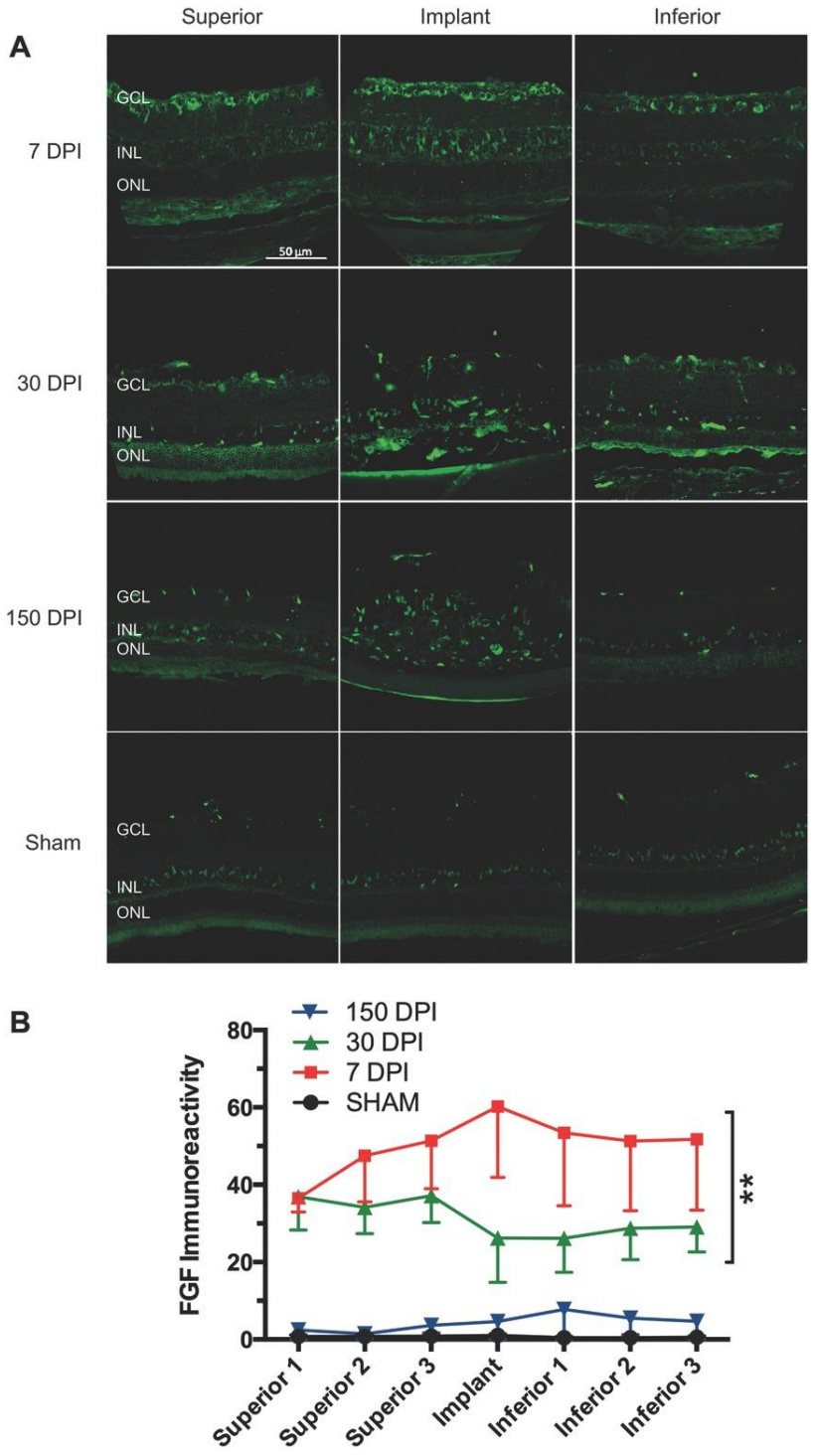

Figure 6. Effects of the prosthetic implant on FGF expression in the retina. A) Reconstruction of vertical section of implanted retina stained for FGF2. Retinas were collected 7, 30, and 150 DPI. Images were acquired from corresponding fields in the different retinas by taking the implant as reference point. B) FGF expression was quickly upregulated after surgery and slowly decreased with time. The fluorescence intensity, measured throughout the retina, shows highly significant differences in FGF immunoreactivity at 7 and 30 DPI compared with either sham-operated or implanted animals at 150 DPI. One-way ANOVA/Tukey's test ($n = 9$ per experimental group). ** $p < 0.01$ versus respective control or 150 DPI. ONL, outer nuclear layer; INL, inner nuclear layer; GCL, ganglion cell layer.

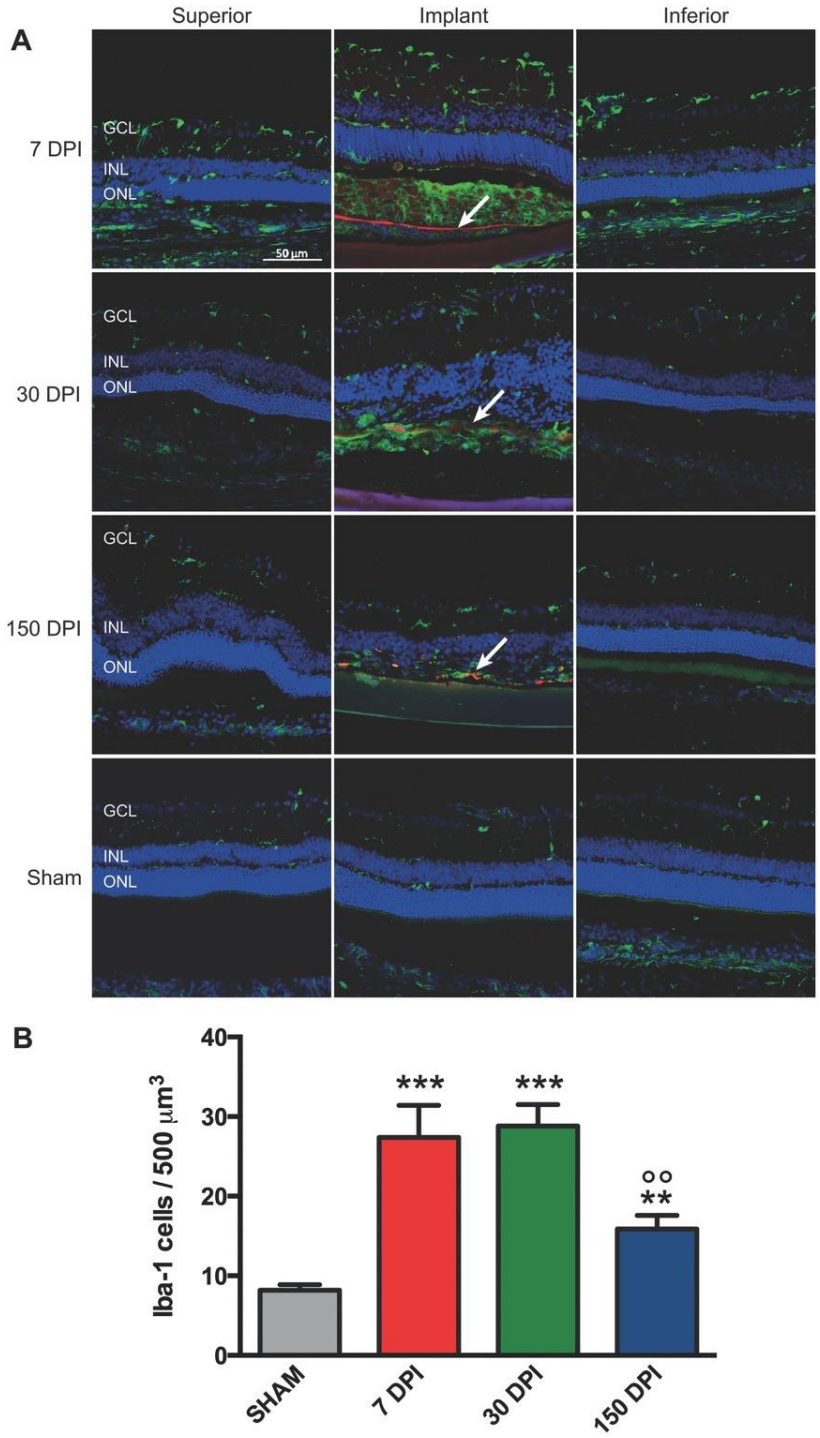

Figure 7. Effects of the prosthetic implant on microglial activation in the retina. A) Panels show transversal sections of retina immunolabeled with Iba-1 antibody (green) and autofluorescence of the polymer (red). Images were acquired from corresponding fields in the different retinas by taking the implant as reference point. Microglial activation was precociously present at 7 DPI; thereafter it persisted in the area of the implant after one month, while it started to decline in the peripheral areas. At 150 DPI, few activated microglia were still visible in the outer retina of the implanted field, but their number was strongly reduced as compared to the earlier stages. B) Quantification of Iba-1 immunoreactivity shows the attenuation of the inflammatory reaction with time postimplant. One-way ANOVA/Tukey's test (n = 9 per experimental group). ** $p < 0.01$; *** $p < 0.001$ versus control; °°$p < 0.001$ versus either 7 or 30 DPI. ONL, outer nuclear layer; INL, inner nuclear layer; GCL, ganglion cell layer.